ADVANCED MATERIALS TECHNOLOGIES
www.advmattechnol.de

Boost and Contraction of Flow by Herringbone Surface Design on the Microfluidic Channel Wall

*Daniele Filippi, Ladislav Derzsi, Francesco Nalin, Andrea Vezzani, Davide Ferraro, Annamaria Zaltron, Giampaolo Mistura, and Matteo Pierno**

The handling of yield-stress fluids typically involves a jammed-to-flow transition that is pivotal for many injection and transport technologies on different scales, such as additive manufacturing, injection molding, food rheology, and oil transport. For all of these applications, it is crucial to be able to tune the fluidization under constant load. The pressure-driven flow of emulsions is reported within a microfluidic channel, one wall of which is patterned by a herringbone-riblet roughness comprising a regular array of V-shaped grooves. With respect to the pressure gradient, this pattern displays a convergent (divergent) orientation that provides a forward (backward) direction. At the tip of the herringbone pattern, the forward and backward flows are almost identical for a viscous Newtonian fluid and a diluted emulsion, whereas a surprising flow boost in the forward direction is observed as the emulsion approaches a jammed state. The flow boost is more effective at small herringbone angles and low pressure loads. 3D velocity profiles along the channel cross-section unravel unexpected heterogeneous stress, band-like distributed, with evidence of nonlocal correlations.

1. Introduction

Many multiphase fluids are commonly yield stress fluids (YSF), which means that they deform elastically as solids until the applied stress reaches a critical value, known as the yield stress σ_Y. Beyond yield, they can flow as liquids; that is, they can deform indefinitely under shear.[1–5] Yielding and flow are widespread in a variety of industrial processes on different scales, including injection molding,[6] 3D printing,[7] embedded droplet printing for drug synthesis,[8,9] smart ferrofluids,[10,11] food technologies,[12] foam stability,[13,14] and drilling mud.[15,16] The transition from solid-like to fluid-like behavior (fluidization) depends critically on the boundary conditions.[17–19] Conversely, clogging is mainly affected by the geometry of the channel, in particular when the flow is constrained by geometries whose width is progressively reduced to a narrow orifice.[20–22]

The flow of YSFs in convergent geometries such as hoppers, funnels, and silos is ubiquitous and has been addressed for a wide variety of dispersed systems, including emulsions,[23–25] foams,[20] granular media,[26,27] and microfluidic crystals.[28–30]

To some extent, the flow of these amorphous materials is independent of their microscopic details and it is characterized by a continuous sequence of elementary plastic events (known as T1), defined as the neighbor swapping of four adjacent constituents.

For a 2D foam, although the flow is driven by a steady pressure gradient, the global mean deformation shows large temporal fluctuations. The decrease in global deformation is correlated with small local cascades of T1 events, while the increase wall friction leads to brittle foam fracture.[20] Furthermore, the spatially averaged normal stress difference is localized in bands with a wavelength on the order of the mean diameter of a bubble.[31] Stress band rupture has been shown to occur at sites of plastic rearrangement avalanche, suggesting local stress relaxation.[32]

For nearly frictionless emulsions, the appearance of clogging at the orifice in quasi 2D hoppers is observed only for narrow openings slightly larger than the diameter of the droplet. Softness is identified as a key factor in controlling clogging; with stiffer particles, clogging is easier.[33] Plastic events tend to occur in small clusters and trigger large fluctuations in droplet deformation, showing that the spatial structure of relaxation of the deformation is related to the local structure.[23,25] Soft particles have also been reported to exhibit a specific surface rheology. In the presence of smooth surfaces, the flow curve shows a kink that is interpreted as a consequence of the slippage of particles on the wall.[19,34,35]

The idea of generating flow patterning to enhance mixing, by simply designing a suitable roughness in the microfluidic channel, has long been known.[36] The flow behavior of Newtonian

D. Filippi, L. Derzsi, F. Nalin, A. Vezzani, D. Ferraro, A. Zaltron, G. Mistura, M. Pierno
Dipartimento di Fisica e Astronomia 'G. Galilei'
Via F. Marzolo 8, 35131 Padova, Italy
E-mail: matteo.pierno@unipd.it

L. Derzsi, F. Nalin
Institute of Physical Chemistry Polish Academy of Sciences
Kasprzaka 44/52, Warsaw 01-224, Poland

The ORCID identification number(s) for the author(s) of this article can be found under https://doi.org/10.1002/admt.202201748

DOI: 10.1002/admt.202201748

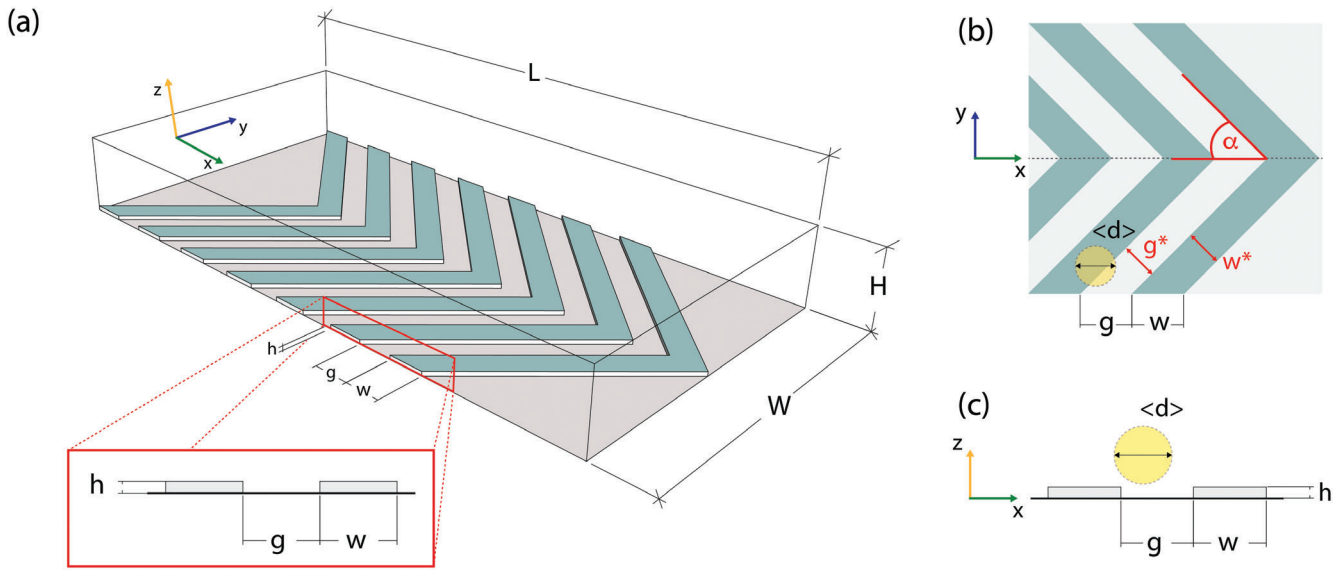

Figure 1. a) 3D outline of the microfluidic channel used to address directional flow. The bottom wall is patterned with V-shaped grooves whose geometry along the longitudinal plane (x, z) direction is expanded in the red box. The size of the channel and that of the grooves are not to scale in the outline. b) Top view of the first grooves of herringbone roughness shown in (a). The angle α is at the intersection of the grooves. The effective (steric) grooves width w^* and gap g^* are compared with the mean size of the emulsion droplets. c) Lateral view corresponding to (b).

fluids in slanted groove and staggered herringbone micromixers has been extensively addressed, showing that the anisotropy of groove patterns allows to engineer flow close to walls.[37–40]

However, the flow of multiphase yield stress fluids in a staggered herringbone roughness has not been considered. In particular, despite extensive evidence that nonlocal fluidization is triggered by surface roughness,[17–19,41–44] the role of directional roughness has not been addressed so far.

In this work, we present a directional roughness based on herringbone texture on one wall of the microfluidic channel. The micrometer scale of the herringbone pattern is designed to interact with the emulsion droplets. The design is highly configurable with respect to the size of the groove, the mutual distance, and the angle at the tip of the V-shape. Having only one wall patterned with directional roughness simplifies the realization of microdevices. In addition, this surface patterning can be easily implemented in parallelizable microfluidics.

The article is organized to first address the directional effects that occur at the intersection of the grooves, considering the role of the V-angle, the pressure load, and the droplet concentration. The velocity profiles along the cross-section of the microfluidic channel are then examined to assess the correlations within the channel.

2. Design of the Directional Microfluidic Roughness

The microfluidic channel is fabricated by multilayer ultraviolet (UV) photolithography, as described in the Fabrication of the microfluidic channels section. The channel has a width $W = 4$ mm, a height $H = 120$ μm and a length $L = 5$ cm. One wall is textured on the micrometer scale with grooves that feature the herringbone pattern, as shown in **Figure 1**.

The grooves are designed to have a height $h = 2.5$ μm and a V-shaped geometry with a groove size w^* and a gap g^* between the grooves tuned so that, along the flow direction x, the longitudinal size w and the gap g are $w = g = 25$ μm independently of the angle of the herringbone α (see details in **Table 1** within the Fabrication of the microfluidic channels section). The microfluidic channel is filled with emulsion droplets whose mean size $\langle d \rangle$ is comparable to the size w of the groove, so on average there are only a few droplets within the gap g of consecutive grooves (see Figure 1c).

Regarding microfluidic confinement, the channel height is approximately ten times the mean droplet size, similar to previous studies.[17,18,30,42,43]

We point out that the roughness height h is only ≃2% of the channel height H, a value that is 5–25 times lower than the roughness height in herringbone micromixers.[36,39,40]

3. Results and Discussion

We first address the directional flow effects that occur at the tip of the herringbone pattern, located at the center $y = 0$ of the channel cross-section. We consider the role that geometry and external forcing play. In Section 3.2, we report a 3D map of the velocity profiles along the cross-section of the channel.

Table 1. Summary of the V-shaped pattern.

A [deg]	w, g [μm]	w^*, g^* [μm]
30	25–25	12–12
45	25–25	18–18
60	25–25	21–21
90	25–25	25–25

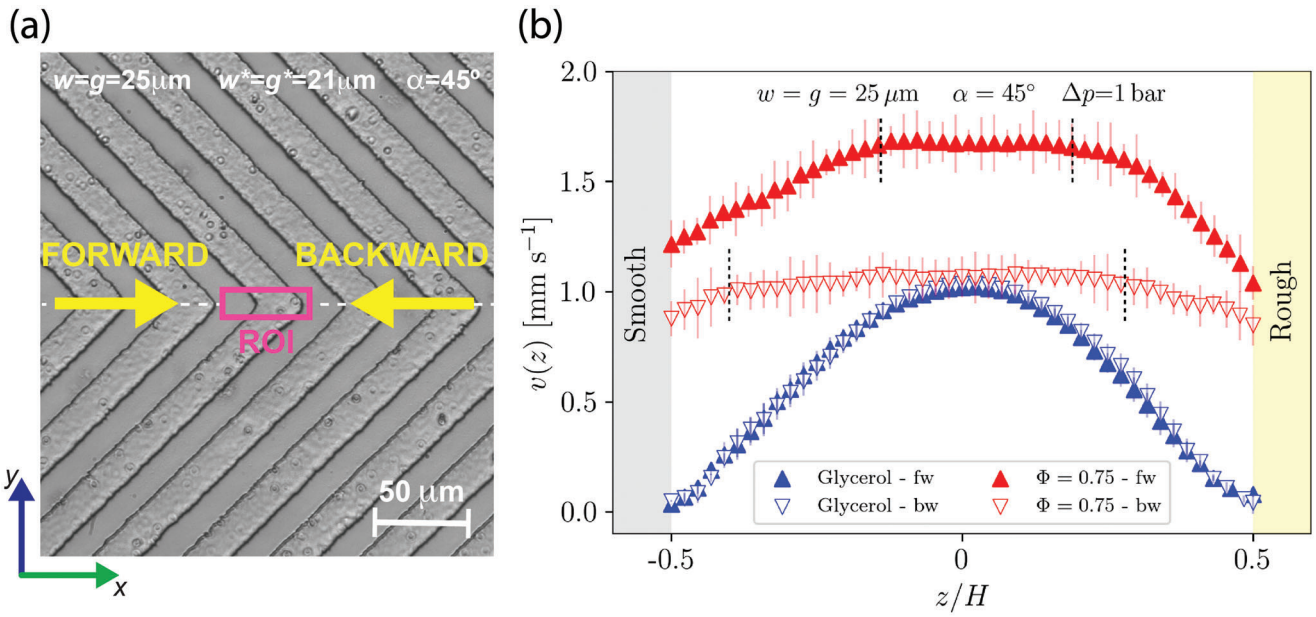

Figure 2. a) Top view of the herringbone pattern taken by optical microscopy with a 60× objective. The flow directions are shown by the yellow arrows. The box is the region of interest (ROI) where the flow is measured. b) Velocity profiles v (z) measured for glycerol (blue data) and the emulsion (red data) in the forward (filled upside triangles) and backward (open downside triangles) directions. Vertical dashed lines on the emulsion flows mark the emulsion plug region.

3.1. Directional Flow on the V-Tip

The velocity profiles v (z, y) are measured by adapting the particle tracking velocimetry (PTV) described in ref. [42,43,45] to scan the channel cross-section (z, y) with a motor resolution of 0.025 µm on z and 1 µm on y. The experimental details are reported in the 3D velocimetry section. Regarding the flow direction x set by the pressure gradient, the herringbone pattern has a convergent (divergent) orientation that can define a forward (backward) direction, as shown in **Figure 2**a.

3.1.1. Newtonian Flow

We first consider the flow of a Newtonian fluid (pure glycerol) flowing in the microfluidic channel whose herringbone texture is set to have an angle $\alpha = 45°$ and a geometry set by $w = g = 25$ µm. We point out that the design of Figure 1 is not the herringbone mixer that would have required a staggered pattern.[36,40] In contrast, in the present description, the V-grooves are aligned along the central axis of the channel. The flow is driven by a pressure load $\Delta p = 1$ bar, set with an accuracy of a few mbar along the longitudinal x direction. It is collected in a region of interest (ROI) whose size is (35 × 7) µm^2 located in the center of the cross-section, small enough compared to the channel size to be considered a local probe in the transverse direction y.

Pure glycerol velocity profiles are reported in Figure 2b as a function of the height of the channel z. Both profiles have the characteristic Poiseuille shape, typical of microfluidics, that is, laminar flow with no signs of turbulence (the Reynolds number is $\simeq 10^{-5}$). Within the error bars, the profiles are essentially the same at all z-stacks, either in the forward or backward direction.

3.1.2. Emulsion Flow

To assess the response of a YSF to the herringbone roughness, textured on the scale of its elementary constituent, we consider a concentrated emulsion as a model system. The emulsion is prepared by dispersing silicone oil in an aqueous phase as described in the Emulsion preparation and characterization section. The result is a thick fluid with an oil droplet concentration that occupies the volume fraction $\Phi = 0.75$. In particular, the emulsion is prepared to have a mean droplet diameter $\langle d \rangle$ comparable to that of the roughness. In units of mean droplet size, the result is: $w/\langle d \rangle = g/\langle d \rangle = 2.65$, and $h/\langle d \rangle \simeq 0.2$ (see Figure 1b,c). Within this configuration, we note that the herringbone roughness is considerably lower than the mean diameter of the droplets.

Interestingly, at the same pressure load for both forward and backward directions, the velocity profiles v (z) taken in the center $y = 0$ of the channel width W are different depending on the flow direction, as shown in Figure 2b. In both forward and backward directions, the velocity profile of the emulsion close to the center of the channel (usually referred to as the plug region) is flattened. The plug-flow originates from the specific stress profile within the channel: between infinitely large parallel walls, the stress decreases linearly from the walls, falling below the emulsion yield stress σ_Y in the center of the channel. In that region, the emulsion flows at constant velocity like an elastic solid, forming a central unyielded plug between two fluidized layers near the walls. Actually, the apparent flow of this solid plug is due to the flow of the surrounding emulsion layers adjacent to the wall (see Figure 8a).

To quantify the difference in the forward and backward flow, we define the maximum velocity v_{max} as

$$v_{max} = v(z_{max}) \quad (1)$$

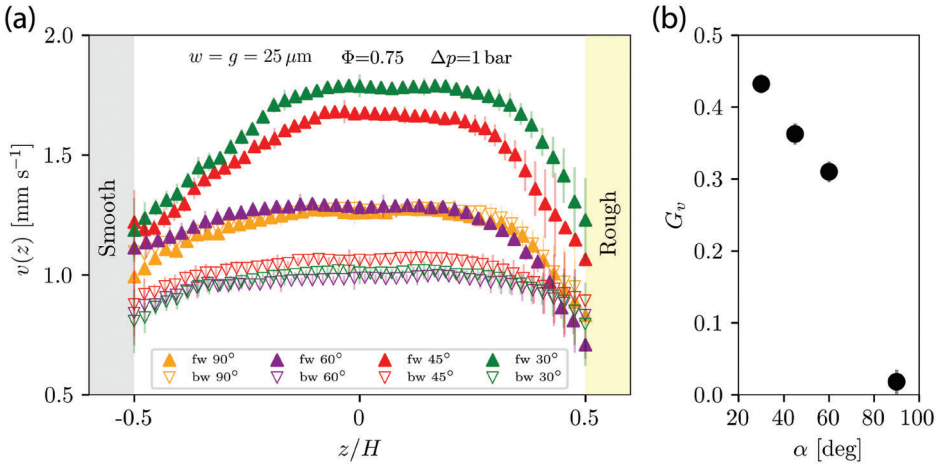

Figure 3. a) Velocity profiles v (z) measured for different V-angles at fixed w, g combination, volume fraction, and pressure drop. Filled upside triangles and open downside triangles refer to the forward and the backward directions respectively. Error bars refer relative to the velocity in each z-stack. b) Relative gain G_v defined by Equation (2) for the profiles of panel (a) as a function of the V-angle. Error bars are relative to the reproducibility over different runs in the same flow direction.

where z_{max} is the position within the channel at which the shear rate is null, $\dot{\gamma}(z_{max}) = 0$, $\dot{\gamma}$ being the derivative of the velocity profile $\dot{\gamma}(z) = \mathrm{d}v(z)/\mathrm{d}z$. In the plug regions, like the ones marked in Figure 2b, v_{max} is taken in the center of the plug region, within the error bars of $\dot{\gamma} = 0$.

As reported in Figure 2b the difference from forward to backward flows is maximum in the middle of the channel height $z/H \simeq 0$. In particular, the forward direction is about 50% higher than in the backward direction. By integrating the velocity profile v (z) over the height H of the channel, it results in a flow rate gain of ≈30% at constant pressure load, in favor of forward flows compared to backward flows. Because the plug region travels on the surrounding layer of the emulsion, this is due to a directional boost of the emulsion fluidization.

Notably, similar wall slip velocity is reported in the backward direction on smooth or rough walls, whereas in the forward direction, the wall slip difference between smooth and rough walls is greater. As extensively discussed in several works, the wall slip difference marks the onset of fluidization.[42,43] This is confirmed by the shortening of the plug region in the forward direction with respect to the backward direction. On the rough wall, within the error bars there seems to be a slight difference in the magnitude of wall slip for the forward direction compared to the backward one.

3.1.3. Effect of the Grooves Angle

To investigate the role played by the herringbone pattern, we consider four patterns with different α: 30°, 45°, 60°, and 90° (see details in Figure 7). A summary of the V-shaped patterns is reported in Table 1 within the Fabrication of the microfluidic channels section. To quantify the relative gain of the flow in the forward direction relative to its opposite, we define the phenomenological parameter

$$G_v = \frac{v_{max}^{fw} - v_{max}^{bw}}{v_{max}^{fw}} = 1 - \frac{v_{max}^{bw}}{v_{max}^{fw}} \quad (2)$$

where v_{max}^{fw} and v_{max}^{bw} are the maximum velocities, as introduced by Equation (1) of the flow in the forward (fw) and backward (bw) directions, respectively.

Given the same pressure load and the same rheology, Equation (2) provides a practical quantity independent of the specific shape of the velocity profiles, which accounts for the relative increase of flow in one direction relative to its opposite. **Figure 3**a reports the velocity profiles of the emulsion at Φ = 0.75 collected within the same ROI shown in Figure 2, by decreasing the V-angle α from $\alpha = 90°$ (no herringbone) to $\alpha = 30°$.

The absence of the herringbone pattern ($\alpha = 90°$) clearly implies the absence of gain $G_v = 0$ within the error bars. As shown in Figure 3b, as α decreases, forward flows increase while backward flows decrease, opening a gap between forward and backward flows. In detail, as α decreases, the backflow decreases less than the forward flow increases. The net result is that the closer the V-shape ($\alpha = 30°$), the higher the relative gain G_v of the forward flow relative to the backward flow. This implies an effective flow boost (frustration) in the forward (backward) direction, in contrast to the absence of the herringbone design. It is noteworthy that the opening of the flow gap does not occur continuously in both directions. In fact, at $\alpha = 60°$ here is no gain in the forward direction, while a significant loss in the backward direction appears. In contrast, for $\alpha < 60°$ the backward flows do not decrease any more, while the forward boost continuously increases as α increases.

3.1.4. Role of the Pressure Load and the Volume Fraction

We address the role played by the pressure gradient by maintaining the same geometry as reported in Figure 2a. Clearly, when pressure forcing increases, the flow velocity increases accordingly in both forward and backward directions, as shown by the trend of v_{max} in **Figure 4**a. However, when pressure changes, this increase is not the same in both directions. In particular, at low pressure (200 and 500 mbar) no sign of directionality appears. Interestingly, as the pressure load increases, the relative flow gain

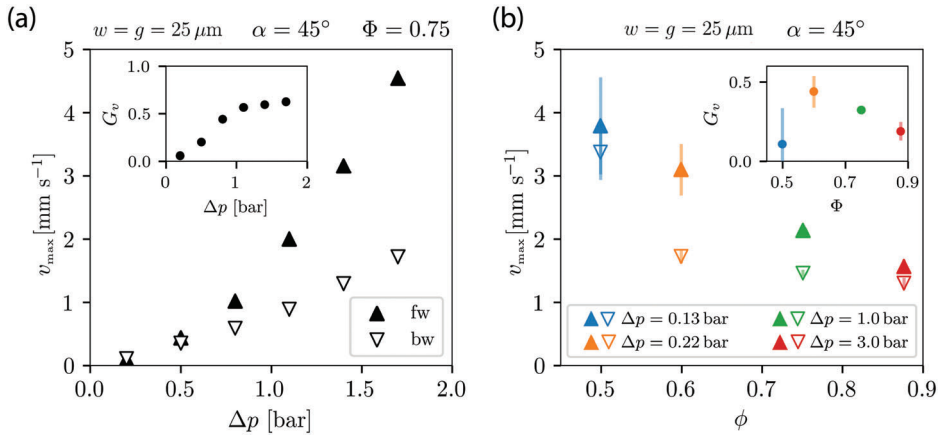

Figure 4. a) Maximum velocity of the emulsion flow at $\Phi = 0.75$ as a function of different pressure loads for the forward (filled upside triangles) and the backward (open downside triangles) flows. The corresponding relative difference is plotted in the inset. b) Maximum velocity of emulsion flow at different volume fractions in the forward (filled upside triangles) and backward (open downside triangles) directions. The corresponding flow gain G_v is shown in the inset as a function of the volume fraction Φ.

G_v increases only until $\Delta p \simeq 1$ bar. For larger pressure loads, it saturates to a nearly constant value (see the inset of Figure 4a), which means that the directional roughness is already effective at low pressure, as wall fluidization begins to develop.

It is not immediate to compare the directional flows of the emulsions for different Φ because a change in volume fraction also affects rheology (see Figure 8a). As a consequence, given the constant pressure gradient, the yield stress σ_Y changes with changing Φ, and this, in turn, affects the flows and therefore the directional boost. To unravel this knot, the pressure load has been adjusted so that at each Φ the emulsion has the same wall slip on the smooth wall. This implies that the wall stress on the smooth wall is the same,[19,35] at least within the experimental resolution. Given the above, the data in Figure 4b show that G_v is practically zero within the error bars for the most diluted emulsion at $\Phi = 0.5$, it reaches a maximum when Φ is approaching the yield and gradually decreases for more concentrated emulsions. This indicates that the presence and concentration of droplets play a crucial role in promoting the directional boost. We point out that the emulsion flow for $\Phi < 0.5$ is not reliable within our setup: indeed, at the lowest pressure settable by the microfluidic controller, the flow velocity is at the limit of the camera frame rate.

3.2. Flow Profiles along the Channel Cross-Section

It is of primary importance to understand whether flow boosting depends on the position along the channel cross-section. Similarly, to what was performed for flows taken in the center $y/W = 0$ of the channel cross-section, we compared the emulsion flows with Newtonian flows, both taken along the cross-section $v(z, y)$ at different y within the local resolution of the ROI.

This comparison is crucial to evaluate the relevance of twisted transverse flows in a channel with obliquely oriented ridges patterned on one wall.[36]

To this end, considering that the herringbone pattern is symmetric with respect to the longitudinal x axis, in **Figure 5**a we report forward and backward flows of pure glycerol along half of the channel cross-section, from the center $y/W = 0$ to the vicinity of the lateral wall $y/W \simeq 0.5$. Within the experimental resolution, the flows of pure glycerol are consistent, forward or backward, regardless of the lateral position y.

This implies a uniform stress distribution within the channel cross-section for both directions. For comparison with the Newtonian reference, we consider the emulsion at $\Phi = 0.6$, which is the most diluted emulsion for which the flow gain is observed. Unlike the Newtonian reference, the emulsion flows in the forward and backward directions are clearly different along the transverse direction y. Within the range $0 \le y/W \lesssim 0.2$, forward flows are always faster than backward flows, as shown in Figure 5b. In particular, at $y/W = 0$ the flow difference is maximum, rapidly decreasing as the distance from the tip of the V-grooves increases along the transverse direction y. Surprisingly, at distances $y/W \gtrsim 0.2$ there is a crossover, and the backflows are faster. This is a consequence of the simultaneous increase in backflows and the decrease in front flows that occur for $y/W > 0.2$, that is, after about 1/2 the width of the hemichannel (see **Figure 6**, top panel). In other words, as the lateral walls are approached, the flow boost takes place in the backward direction, opposite to what happens in the center of the channel cross-section. Independently of the specific direction of the boost with respect to the orientation of the herringbone pattern, the stress distribution appears to be long-correlated along the transverse direction y, up to about the middle of the channel hemi-width $y/W \simeq 0.25$. Furthermore, the stress along the cross-section is clearly heterogeneous for the emulsion with respect to the Newtonian fluid.

Bottom panel of Figure 6 reports the position of v_{max}, as defined by Equation (1), for the emulsion flow along the y-direction. Interestingly, the flow boost appearing in the top panel is correlated with the shift of the position of v_{max} reported in the bottom panel, with the only exception observed at $y/W \simeq 0.1$ caused by the noise of the experimental velocity profile.

3.3. Discussion

A detailed understanding of the mechanism that drives the increase in fluidity for a specific flow direction is beyond the scope

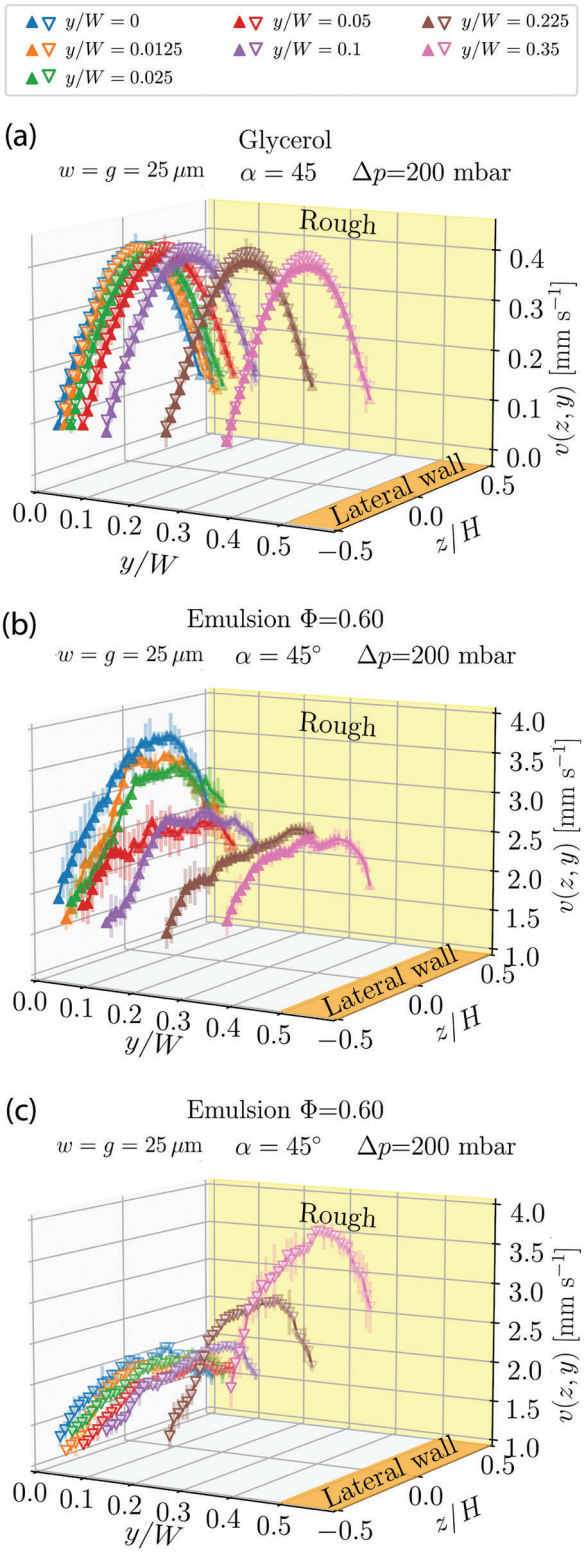

Figure 5. Velocity profiles along the cross-section (y, z) of the microfluidic channel. The position of the herringbone pattern is marked by the yellow wall, at $z/H = 0.5$. The position of the lateral wall is marked by the orange box, at $y/W = 0.5$. a) Pure glycerol flows. b,c) Emulsion at $\Phi = 0.6$ flowing in the b) forward and c) backward directions.

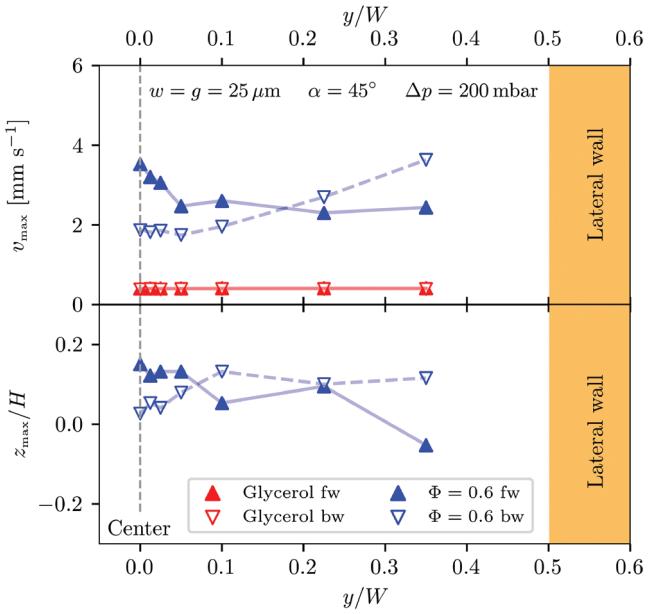

Figure 6. Top Panel: Maximum velocity (Equation (1)) of the emulsion (blue symbols) and glycerol (red symbols) flowing in the forward (filled upside triangles) and backward (open downside triangles) directions as a function of the normalized lateral position. Bottom Panel: Position of the maximum velocity for the emulsion flowing in the forward and backward directions. The derivative of the velocity profiles $v(z)$ reported in Figure 5 is taken after polynomial smoothing of the experimental values due to the noise affecting the velocity.

of this work. Indeed, since directional patterns occurring in the V-tip extend in the transverse direction with respect to the flow, a comparison with models should require 3D resolution, which is usually complex to implement, and should be benchmarked in a dedicated work.

As extensively debated in the last decade, it is not possible to directly link velocity profiles with emulsion rheology, as the relation between local stress and local shear rate cannot be explained by a unique master curve in microfluidic confinement, in the presence of different boundary conditions on the channel walls.[17–19,42,43,46,47] These observations result in a "nonlocal" fluidity that describes how the plastic activity spreads spatially throughout the system due to nonlocal elastic relaxation: it accounts for a spatial length scale at which the cooperativity is involved in the plastic activity during flow.[17,18,43] Data shown in Figure 4b confirm the crucial role that the presence of droplets and their plastic arrangements play in the boost effect. Interestingly, the volume fraction close to the onset of the cooperativity length is indeed the one for which the flow gain is maximum, given the same wall slip for all volume fractions. At a higher volume fraction, while the cooperativity length increases, the bulk viscosity and the yield stress increase as well, so that at constant applied stress the flow gain is lower.

Furthermore, it is well known that the stress profile is linear in the Poiseuille flow between infinite parallel plates with the same boundary conditions, being zero at half the height of the channel.[48–50] At variance, in the presence of different boundary conditions between the walls, like, e.g., the case of smooth and rough walls, the wall stress results to be different. As a

consequence, all the stress profile is shifted toward the wall with the larger stress. Accordingly, the position of zero stress is shifted with respect to the center of the channel height.[42,50] For this reason, the plug regions of the velocity profiles marked in Figure 2b are not symmetric with respect to $z/H = 0$.

Similarly, Figure 6 shows that the presence of flow boost is clearly associated with a shift of the position of v_{max} triggered by the roughness textured on one wall of the channel. Notably, this difference reflects a shift of the zero-stress position changes along the channel cross-section, resulting in longitudinal stress banding. This induces a flow heterogeneity along the cross direction similar to that reported for T1 droplet rearrangements in hopper flows[22–25,33] and stress banding in compressed 2D foam,[31] but at a lower volume fraction.

The reported phenomenology accounts for the complex interplay that involves external forcing Δp, yield stress σ_Y, spatial cooperativity, and nonlocality.[17,18,43]

Therefore, to address this complexity, a dedicated modeling is necessary, ideally comprising independent experiments on the determination of the directional wall stress.

4. Conclusion and Prospects

In summary, we observed a notable directional fluidization of emulsions flowing through a microfluidic channel that has only one wall textured with a herringbone design. This boost is practically null for a Newtonian viscous fluid and for sufficiently diluted emulsions. In addition, the boost is heterogeneous along the cross-section. Interestingly, by making appropriate design changes, it is possible to tune the boost and promote the filling of thin-wall parts by reducing the flow resistance. In fact, similar strategies have been successfully used to reduce the pressure drop of polymer melts in injection molding.[51–53]

Conversely, concentrated emulsions also play a crucial role in additive manufacturing, where they act as bioinks to print functional materials, often inspired by biological systems.[54] For example, its scaffold structure can serve as a template where cells can grow, with the aim of replicating living tissues.[55,56] Here, the composition of the liquid phases and the size of the droplets determine the physiochemical characteristics of the final material. Microfluidics enabled great control of these parameters; despite this, the intrinsic properties of bioinks limit their accessibility and printability because their non-Newtonian nature can be an obstacle when extruded through a narrow constriction. Materials with attractive characteristics would be discarded due to the increased stress experienced by cells during the printing process or due to the lower printability of a viscoelastic fluid after extrusion.[57]

Finally, directionally induced flow boost is also expected to be relevant for powders and granular matter that show a rheological behavior similar to that of YSF and a transport mechanism strongly influenced by the granular rearrangement.[26,58–60]

In conclusion, it should be noted that the emergence of local stress that extends at a distance much longer than the size of the emulsion droplet, is consistent with the reporting of nonlocal T1 events in the emulsion that flows in convergent geometries.[22–25,33] Although the mechanism of this directional boost still needs to be fully addressed, it appears to be related to the presence of a dispersed phase at the scale at which the roughness produces a directional effect depending on the specific design. We hope that these findings may be a stimulus to address a suitable model (either 2D or 3D) that accounts for the presence of directional flows, likely rooted in the structure of the directional wall rheology.

5. Experimental Section

Fabrication of the Microfluidic Channels: The fabrication procedure for microfluidic channels was similar to that used in refs. [42,43] to realize channels characterized by a microroughness made of parallel grooves. The groove-patterned surfaces were manufactured by a standard photolithographic technique; negative photoresist SU-8 2002 was spun onto a clean 75×50 mm^2 glass slide using a spin coating procedure (1500 rpm for 30 s) to form a 2.5 μm thick layer. After baking at 95 °C for 1 min, the photoresist layer was covered with a printed photomask and exposed to UV light. The mask was then removed and the glass slide was baked again at 95 °C for 2 min. The micropattern was obtained by washing the uncured resist with the photoresist developer for 2 min. The channel was then assembled using as top walls a microscope slide that was drilled to apply the tubes for inlets and outlets. To close the channel, a 120 μm thick dry photoresist film (WBR-2000, DuPont, USA) was used. The dry photoresist acts both as a glue to bond the top and bottom glass slides and as a side wall of constant height. The dry photoresist was cut into a channel shape using a knife plotter (Craft Robo CC200-20, Graphtec, Japan) and then laminated to the glass plate, removing trapped air bubbles. To complete the bond procedure, the sample was placed under a hydraulic press for 5 min at 80 °C with a pressure of 2 bar. With this step, the cover plate was preboned to the cover glass. Finally, to fix the different layer and polymerize the photoresist, the sample was exposed to UV light (i-line 365 nm) for 60 s.

Different combinations of gaps and widths ranging from the summarized in Table 1 were fabricated.

Roughness Characterization: To assess the quality of the microgrooves, an optical profilometer (SENSOFAR S neox, Spain) was used. Structures showed sharp edges and surfaces had a mean roughness of 150 nm that was negligible with respect to height ($h = 2$ μm). In **Figure 7**a–c profilometer scans are reported for the three angles used in the experiment. Figure 7d shows the profile extracted for the herringbone grooves with $w = g = 25$ μm and $\alpha = 45°$.

Surface Modification: A hydrophilic coating was applied to the inner walls of the microfluidic channel to homogenize the wetting properties of the surfaces and to avoid adhesion and coalescence of the oil droplets on the walls. The coating was achieved by treating the closed microfluidic chip with an oxygen plasma to activate the inner surfaces for 1 min at 300 W and an oxygen flow of 35 sccm. Then a 2.5% (w/w) PVP (polyvinylpyrrolidone K90, AppliChem) water solution was flowed within the channel for at least 2 h with a flow rate of 1.5 mL h^{-1} using a syringe pump. After treatment, the channel was rinsed by flushing 5 mL of MilliQ water at a flow rate of 2.5 mL h^{-1} to remove the excess PVP and dried with nitrogen flow at a pressure of ≈1 bar.

Emulsion Preparation and Characterization: The nonadhesive concentrated emulsion was prepared by mixing silicone oil (Rhodosil 47 v 1000, bluestar Silicones, France) and the aqueous phases using a custom spatula mixer. The latter consisted of a mixture of glycerine (Sigma-Aldrich, Germany) and MilliQ water (54% wt glycerine, 46% wt water) stabilized by 1% wt of tetradecyltrimethyl-ammonium bromide (TTAB). The surfactant led to a nonadhesive emulsion and increased the stability of the emulsion by preventing the coalescence of droplets under pressure driven flow inside the microfluidic channel. The continuous phase was seeded with diluted suspension (0.002% wt) of fluorescent nanoparticles (FluoSpheres, ThermoFisher, USA) of size $d \approx 0.2$ μm which were used as tracers during Particle Tracking Velocimetry measurements. The emulsification process began with the addition of silicone oil at a slow pace (≈1 mL min^{-1}) to the continuous phase with a spatula rotation speed of ≈1 Hz. The addition continued until the volume fraction of oil

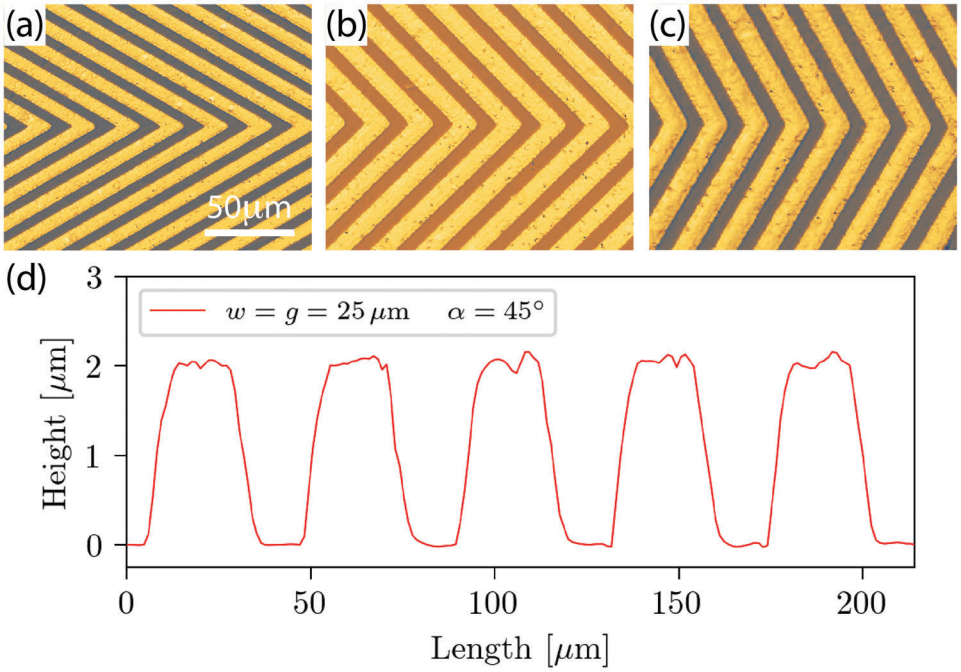

Figure 7. Profilometer scans for a) $\alpha = 30°$, b) $\alpha = 45°$, and c) $\alpha = 60°$. d) Representative height profile shown only for pattern (b): $w = 25$ μm, $g = 25$ μm, and $\alpha = 45°$.

relative to the total mixture was approximately $\Phi = 0.93$. At this Φ the emulsion was unstable. Therefore, to avoid droplet coalescence, the emulsion was diluted with the same continuous phase at a volume fraction of $\Phi = 0.875$.

Emulsion Rheology: At the end of the emulsification process, the obtained emulsion was characterized by rheological and microstructural information. Rheological characterization was performed with a cone plate rheometer (Kinexus lab + Netzsch, Germany) that imposes rotational velocity (that is, shear rate, $\dot{\gamma}$) and measures torque (that is, shear stress, σ). The collected curves σ versus $\dot{\gamma}$ curves are reported in **Figure 8**a. The mean diameter $\langle d \rangle$ and the size distribution of the emulsion were measured using an optical method; a small sample of the emulsion was diluted in an aqueous solution of 1% TTAB, then a few drops of the diluted emulsion were placed between two microscope cover slips and a large number of optical images were taken under a bright field optical microscope with a 100× magnification objective (see Figure 8b). The images are then analyzed using the FIJI software[61] that measures approximately the diameter of 8500–10 000 oil droplets. From the analysis, the mean diameter of the droplet d and the polydispersity (coefficient of variance $CV = \sigma/d \times 100\%$) are determined. Measurements are repeated a few times to test the stability of the emulsion. During the period in which the experiments take place, no noticeable differences are observed.

Velocimetry: The experimental setup of micro-Particle Tracking Velocimetry consisted of a motorized inverted microscope (Eclipse Ti-E, Nikon, Japan) coupled to a sCMOS camera (Zyla 5.5, Andor, UK). A 60× magnification objective (SuperPlan Fluo, Nikon, Japan) was used, corrected apochromatically, with a long working distance WD = 2 mm, and a numerical aperture NA = 0.7 whose vertical position (z-axis) can be fine-tuned with a step resolution of 0.025 μm.

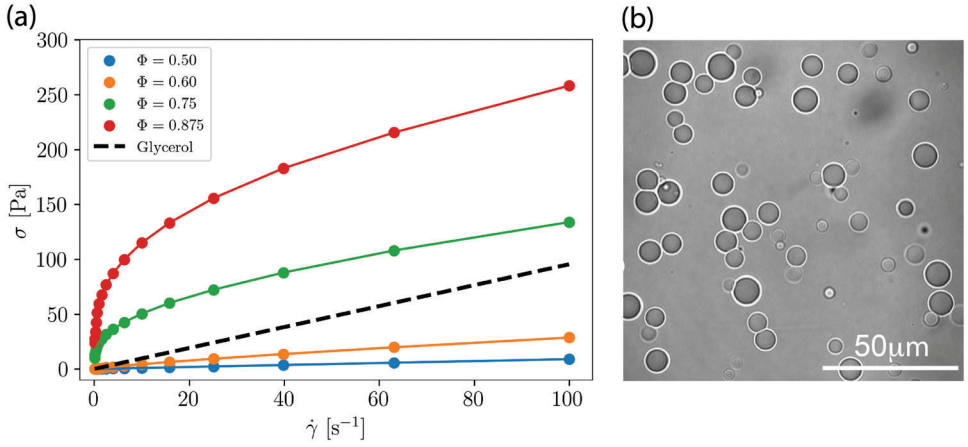

Figure 8. a) Shear stress σ as a function of the shear rate $\dot{\gamma}$ for emulsions at different volume fractions Φ. Dashed line is the rheological curve of pure glycerol (Newtonian reference). b) Diluted emulsion imaged with a 60× microscope objective.

The depth of field of the microscope objective was ≃1.5 µm. The microscope was equipped with high-speed motorized *x,y* scanning stages (Thorlabs, Germany) that allowed the microfluidic channel to move in the *x,y* plane with a spatial resolution of 1 µm. The emulsion inside the channel was illuminated with a Diode-Pumped Solid-State (DPSS) laser beam with a wavelength of 532 nm and a maximum power of 5 mW.

Stacks of 500 fluorescence images of tracers dispersed in the continuous phase of the emulsion are recorded at different heights of the channel, from bottom to top, with 2 µm steps. To collect the complete 3D scan of the flow, velocity profiles were recorded repeating the *z*-scan at different positions along the *y* axis. In doing so, the measure $v(z, y)$ was taken as a function of both the height of the channel *z* and the width of the channel *y*, in which the ROI was located, and was referred to it as a 3D scan. Statistical error on each *z*-stack was computed on hundreds of tracks. For the emulsion flow, it was small in the plug region because of narrow velocity distribution. Conversely, it was larger close to the wall because of the presence of plastic rearrangements that broaden the velocity distribution.

Flow Control: The emulsion flow was pressure controlled using a Microfluidic Flow Control System (MFCS seriesfrom Fluigent, France) by applying a differential pressure between the input and outlet of the channel with a precision of ±5 mbar in the range 1–3000 mbar.

Acknowledgements

Lucia Villanova and Isabella Zanellato are warmly thanked for help with the experimental measures, Giorgio Delfitto for technical assistance, and Giacomo Pierno for support with graphics. The authors are indebted with Francesca Pelusi and Mauro Sbragaglia for invaluable discussions and Piotr Garstecki for granting access to microfabrication facilities. Partial funding from BIRD 2021 "BiodivSeq" of Padua University and PRIN 2017 "UTFROM" of the Italian Ministry of University and Research is kindly acknowledged. F.N. acknowledges funding from the European Union's Horizon 2020 research and innovation program under the Marie Sklodowska-Curie Grant Agreement No. 813786 (EVOdrops). D.F. acknowledges funding from Programma Operativo Nazionale (PON) "Ricerca e Innovazione" 2014–2020 (ReactEU-RUAPON-Viganov) of the Italian Ministry of University and Research. L.D. acknowledges the support from the Foundation for Polish Science under the TEAM-NET programme (project No. POIR.04.04.00-00-16ED/18).

Conflict of Interest

The authors declare no conflict of interest.

Data Availability Statement

The data that support the findings of this study are available from the corresponding author upon reasonable request.

Keywords

directional roughness, fluidization, microfluidic flow, nonlocality, wall slip, yield-stress-fluids

Received: October 15, 2022
Revised: March 31, 2023
Published online:

[1] Y. M. Joshi, G. Petekidis, *Rheol. Acta* **2018**, *57*, 521.
[2] A. Z. Nelson, K. S. Schweizer, B. M. Rauzan, R. G. Nuzzo, J. Vermant, R. H. Ewoldt, *Curr. Opin. Solid State Mater. Sci.* **2019**, *23*, 100758.
[3] T. Divoux, D. Tamarii, C. Barentin, S. Manneville, *Phys. Rev. Lett.* **2010**, *104*, 208301.
[4] P. Coussot, G. Ovarlez, *Eur. Phys. J. E* **2010**, *33*, 183.
[5] D. Bonn, M. M. Denn, *Science* **2009**, *324*, 1401.
[6] U. M. Attia, S. Marson, J. R. Alcock, *Microfluid. Nanofluid.* **2009**, *7*, 1.
[7] C. Perrinet, E. J. Courtial, A. Colly, C. Marquette, R. Fulchiron, *Adv. Mater. Technol.* **2020**, *5*, 1901080.
[8] A. Z. Nelson, B. Kundukad, W. K. Wong, S. A. Khan, P. S. Doyle, *Proc. Natl. Acad. Sci. U. S. A.* **2020**, *117*, 5671.
[9] A. Z. Nelson, J. Xie, S. A. Khan, P. S. Doyle, *Adv. Mater. Technol.* **2021**, *6*, 2001245.
[10] Y. P. Seo, S. Han, J. Choi, A. Takahara, H. J. Choi, Y. Seo, Y. P. Seo, S. Han, J. Choi, Y. Seo, A. Takahara, H. J. Choi, *Adv. Mater.* **2018**, *30*, 1704769.
[11] C. Rigoni, S. Bertoldo, M. Pierno, D. Talbot, A. Abou-Hassan, G. Mistura, *Langmuir* **2018**, *34*, 9762.
[12] A. Sun, S. Gunasekaran, *Int. J. Food Prop.* **2009**, *12*, 70.
[13] A. Salonen, *Curr. Opin. Colloid Interface Sci.* **2020**, *50*, 101381.
[14] D. A. Sessoms, H. Bissig, A. Duri, L. Cipelletti, V. Trappe, *Soft Matter* **2010**, *6*, 3030.
[15] P. R. de Souza Mendes, R. L. Thompson, *Curr. Opin. Colloid Interface Sci.* **2019**, *43*, 15.
[16] N. Liu, D. Zhang, H. Gao, Y. Hu, L. Duan, *Sensors* **2021**, *21*, 3592.
[17] J. Goyon, A. Colin, G. Ovarlez, A. Ajdari, L. Bocquet, *Nature* **2008**, *454*, 84.
[18] V. Mansard, L. Bocquet, A. Colin, *Soft Matter* **2014**, *10*, 6984.
[19] J. R. Seth, C. Locatelli-Champagne, F. Monti, R. T. Bonnecaze, M. Cloitre, *Soft Matter* **2012**, *8*, 140.
[20] B. Dollet, C. Bocher, *Eur. Phys. J. E* **2015**, *38*, 123.
[21] B. Dollet, A. Scagliarini, M. Sbragaglia, *J. Fluid Mech.* **2015**, *766*, 556.
[22] G. L. Hunter, E. R. Weeks, *Rep. Prog. Phys.* **2012**, *75*, 066501.
[23] D. Chen, K. W. Desmond, E. R. Weeks, *Phys. Rev. E* **2015**, *91*, 62306.
[24] D. D. Chen, K. W. Desmond, E. R. Weeks, *Soft Matter* **2012**, *8*, 10486.
[25] X. Hong, K. W. Desmond, D. Chen, E. R. Weeks, *Phys. Rev. E* **2022**, *105*, 014603.
[26] L. Vanel, P. Claudin, J. P. Bouchaud, M. E. Cates, E. Clement, J. P. Wittmer, *Phys. Rev. Lett.* **2000**, *84*, 1439.
[27] S. Tewari, B. Tithi, A. Ferguson, B. Chakraborty, *Phys. Rev. E* **2009**, *79*, 11303.
[28] Y. Gai, A. Bick, S. K. Y. Tang, *Phys. Rev. Fluids* **2019**, *4*, 014201.
[29] P. Garstecki, G. M. Whitesides, *Phys. Rev. Lett.* **2006**, *97*, 024503.
[30] E. Tamborini, L. Cipelletti, L. Ramos, *Phys. Rev. Lett.* **2014**, *113*, 078301.
[31] B. Behera, C. Kalelkar, K. Raj M, *Phys. Fluids* **2019**, *31*, 082111.
[32] F. Pelusi, M. Sbragaglia, R. Benzi, *Soft Matter* **2019**, *15*, 4518.
[33] X. Hong, M. Kohne, M. Morrell, H. Wang, E. R. Weeks, *Phys. Rev. E* **2017**, *96*, 062605.
[34] S. P. Meeker, R. T. Bonnecaze, M. Cloitre, *Phys. Rev. Lett.* **2004**, *92*, 198302.
[35] S. P. Meeker, R. T. Bonnecaze, M. Cloitre, *J. Rheol.* **2004**, *48*, 1295.
[36] A. D. Stroock, S. K. W. Dertinger, A. Ajdari, I. Mezic, H. A. Stone, G. M. Whitesides, *Science* **2002**, *295*, 647.
[37] A. Glia, P. Sukumar, A. T. Brimmo, M. Deliorman, M. A. Qasaimeh, *Microfluidics, BioMEMS, and Medical Microsystems XVII*, Vol. *108751F*, SPIE BiOS, San Francisco, California, USA, **2019**, pp. 207-213, https://doi.org/10.1117/12.2516035.
[38] S. P. Kee, A. Gavriilidis, *Chem. Eng. J.* **2008**, *142*, 109.
[39] V. J. Shenoy, C. E. Edwards, M. E. Helgeson, M. T. Valentine, *BioTechniques* **2021**, *70*, 285.
[40] A. D. Stroock, S. K. Dertinger, G. M. Whitesides, A. Ajdari, *Anal. Chem.* **2002**, *74*, 5306.
[41] J. Paredes, N. Shahidzadeh, D. Bonn, *Phys. Rev. E* **2015**, *92*, 042313.
[42] L. Derzsi, D. Filippi, G. Mistura, M. Pierno, M. Lulli, M. Sbragaglia, M. Bernaschi, P. Garstecki, *Phys. Rev. E* **2017**, *95*, 6.

[43] L. Derzsi, D. Filippi, M. Lulli, G. Mistura, M. Bernaschi, P. Garstecki, M. Sbragaglia, M. Pierno, *Soft Matter* **2018**, *14*, 1088.
[44] F. Pelusi, M. Sbragaglia, A. Scagliarini, M. Lulli, M. Bernaschi, S. Succi, *Europhys. Lett.* **2019**, *127*, 34005.
[45] L. Brigo, M. Natali, M. Pierno, F. Mammano, C. Sada, G. Fois, A. Pozzato, S. Dal Zilio, M. Tormen, G. Mistura, *J. Phys. Condens. Matter* **2008**, *20*, 354016.
[46] A. Nicolas, J. Barrat, *Phys. Rev. Lett.* **2013**, *110*, 138304.
[47] J. Goyon, A. Colin, L. Bocquet, *Soft Matter* **2010**, *6*, 2668.
[48] D. J. Tritton, *Physical Fluid Dynamics (Second Edition)*, Oxford University Press, New York, NY, USA **2012**.
[49] R. G. Larson, *The Structure and Rheology of Complex Fluids*, Oxford University Press, New York **1999**.
[50] A. Vayssade, C. Lee, E. Terriac, F. Monti, M. Cloitre, P. Tabeling, *Phys. Rev. E* **2014**, *89*, 052309.
[51] D. Masato, M. Sorgato, M. Babenko, B. Whiteside, G. Lucchetta, *Mater. Des.* **2018**, *141*, 286.
[52] D. Masato, M. Sorgato, A. Batal, S. Dimov, G. Lucchetta, *Polym. Eng. Sci.* **2019**, *59*, 1889.
[53] L. Orazi, M. Sorgato, L. Piccolo, D. Masato, G. Lucchetta, *Lasers Manuf. Mater. Process.* **2020**, *7*, 207.
[54] A. Khademhosseini, R. Langer, *Nat. Protoc.* **2016**, *11*, 1775.
[55] J. M. de Rutte, J. Koh, D. Di Carlo, *Adv. Funct. Mater.* **2019**, *29*, 1900071.
[56] M. Marcotulli, M. C. Tirelli, M. Volpi, J. Jaroszewicz, C. Scognamiglio, P. Kasprzycki, K. Karnowski, W. Święszkowski, G. Ruocco, M. Costantini, G. Cidonio, A. Barbetta, *Adv. Mater. Technol.* **2023**, *8*, 2201244.
[57] D. Chimene, R. Kaunas, A. K. Gaharwar, *Adv. Mater.* **2020**, *32*, 1902026.
[58] R. M. Gandia, F. C. Gomes, W. C. D. Paula, P. J. Aguado Rodriguez, *Powder Technol.* **2021**, *394*, 478.
[59] C. S. Campbell, *Powder Technol.* **2006**, *162*, 208.
[60] F. Ayuga, M. Guaita, P. J. Aguado, A. Couto, *J. Eng. Mech.* **2001**, *127*, 1067.
[61] C. A. Schneider, W. S. Rasband, K. W. Eliceiri, *Nat. Methods* **2012**, *9*, 671.